JOURNAL OF COMPUTATIONAL PHYSICS **131,** 54–69 (1997)
ARTICLE NO. CP965456

Front Tracking for Shear Bands in an Antiplane Shear Model

F. Xabier Garaizar*,[1] and John Trangenstein†,[2]

*Department of Mathematics and Center for Research in Scientific Computation, Box 8205, North Carolina State University, Raleigh, North Carolina 27695; †Department of Mathematics, Box 90320, Duke University, Durham, North Carolina 27706-0320

Received April 7, 1995; revised February 21, 1996

In this paper we describe a numerical algorithm for the study of shear band, formation and growth in two-dimensional antiplane shear. The constitutive model uses a non-associative flow rule. The numerical scheme is based on a Godunov method for updating the velocity, while the stress is updated via integration along particle paths. The scheme is coupled with a front tracking algorithm for careful evolution of the shear bands. The main challenges are the non-hyperbolicity of the shear band formation and growth (front tracking avoids the catastrophic effects of the loss of hyperbolicity in the Godunov-type numerical scheme), the existence of endpoints for the shear band (the tracked front does not separate the computational domain into disconnected regions), and the non-hyperbolic rate of growth of the shear band. We give examples of the success of the algorithm and show convergence tests.

1. INTRODUCTION

The main goal of this paper is to describe an application of front tracking to the numerical resolution of deformations in granular materials with shear bands. The problem we consider relates to two-dimensional shearing, where the motion is homogeneous in the x_3 direction. In previous papers we carried out a preliminary study of tracking of shear bands for one-dimensional problems [6, 11]. In those problems the shear bands were non-hyperbolic fronts, as in the present case. An important difference is that in one dimension the shear band is a point on the real line and separates the computational domain in two disjoint regions; while in two dimensions, the shear band is a curve in the plane which may or may not separate the domain into disjoint regions. Furthermore, the growth of the shear band at the end points presents a new computational challenge: the non-hyperbolic nature of the band means that the evolution of the end points is not controlled by a CFL constraint. For this reason, the interaction of the tracked front with the underlying hyperbolic grid is nontrivial and we develop techniques to allow for the growth of the shear band by more than one cell per time step.

In particular, the model used in this paper includes a non-associative flow rule. Non-associative flow rules are recognized as an important tool in the modeling of deformations in granular materials (see Vardoulakis and Graf [21]). This present model has been studied by Schaeffer [13] and offers a criterion for the formation of shear bands and a description of the evolution of the material inside the band.

The non-associativity of the flow rule implies ill-posedness, in the sense of Hadamard, at certain levels of stress. Schaeffer [13] formulated a relation between ill-posedness and the formation of the shear bands. We will use this formulation in the numerical algorithm described in this paper.

Another feature of non-associative flow rules is the possibility that plastic waves travel faster than elastic waves of the same family. This phenomenon had been previously pointed out by Sandler and Rubin [12] as a potential difficulty for the design of numerical algorithms. As it relates to the algorithm described in this paper, the difficulty lies in the non-existence of solutions to one-dimensional Riemann problems in the coordinate directions. The regions where these solutions may not exist are explored in [5], together with possible modifications to the wave structure (inclusion of plastic shocks) or to the model itself which will eliminate the regions of non-existence while maintaining the ill-posedness conductive to shear banding. At present we wish to focus on the novel application of front tracking to shear band models and not on the model itself. We will assume that the plastic wave speeds are always lower than the elastic wave speeds and, for the examples in this paper, we will check that it is the case when solving Riemann problems in the coordinate directions.

The deformations studied in this paper are governed by the equation of conservation of momentum and the constitutive relations for the material. These constitutive

[1] Supported by NSF Grant DMS 9201115, which includes funds from AFOSR. E-mail address: garaizar@math.ncsu.edu. This paper was written while visiting the Department of Mathematics at Duke University.

[2] Supported by NSF Grants DMS 9201034, DMS 9201361, DMS 9407029, and DOE Grant DE-F605-92-ER25145. E-mail address: johnt@math.duke.edu.

0021-9991/97 $25.00

relations are not expressed in conservation form for plastic deformations. For levels of stress below a certain critical value, the system of equations given by the conservation of momentum and the constitutive relations is hyperbolic, although not in a conservation form, in general. The numerical algorithm used in this paper is of Godunov type for the updating of the velocity (conservation of momentum) and the stress whenever possible (elastic constitutive relations). Otherwise (plastic constitutive relations), the stress is updated with an integration along particle paths (as in [17, 18]).

When the material reaches a critical value of loading, shear banding occurs. While the overall deformation is described by a hyperbolic system of equations, hyperbolicity is lost at the points where shear banding occurs. At these points, the deformation is described by jump relations in a manner similar to shock hugoniots. From a numerical point of view, shear bands are treated as internal boundaries. When a shear band is initiated, the orientation of the band is obtained from a critical loading criteria that provides the direction of planar waves for which ill-posedness first occurs.

Once the shear band is formed, the behavior of the deformation in the regions near the shear band is of primary interest. The shear band may continue to load while simultaneously a relief front propagates from the shear band in the transverse direction [13]. This creates a region of elastic unloading contiguous to the band, although we still expect that the material ahead of the unloading front (including the endpoints of the band) is loading. A sharp resolution of the deformation at the near the shear band is necessary, in order to (a) accurately describe the localization of the deformation around the shear band and (b) accurately establish the growth of the band. Due to the non-hyperbolic nature of the band itself, simple capturing of the fronts does not seem to apply. In our proposed tracking algorithm, the evolution of the shear band is computed separately from the evolution in the rest of the domain, where the deformation is hyperbolic. Both algorithms, the hyperbolic scheme, and the tracking of the front, interact in a non-trivial manner, providing each other with the appropriate flux quantities necessary to perform the time updates at the cells near the shear band and the band itself. This technique was previously tested for a simpler one-dimensional model [6] for which the analytical results were available with great success.

The tracking techniques that we use near the shear band loosely follow those described by Chern and Colella in [2], with modifications to adjust for the properties of the tracked front. A first modification will appear in the treatment of "flux redistribution" near the end points of the band, since at that point there is ambiguity about the meaning of the regions to the left and right of the front. Also since the shear band is not a hyperbolic front, the endpoints could propagate at arbitrary speed and the growth of the band would not be limited by the CFL condition. In particular, an ideal test could be chosen in which the end points propagate at infinite speed. Thus, it is not possible to assume that the end points at the conclusion of a time step are near the position of the end points at the beginning of the time step. To allow the front to propagate at the proper speeds (probably in excess of the material wave speeds), we use an iterative process for fractional time-steps. At the end of each substep only one new cell is allowed to be intersected by shear bands, and during each substep we update all cells where the shear band is likely to grow and those where it already exists. This iterative process, although it seems costly in efficiency, is not so since the iterative process is performed only in regions surrounding the shear bands and potential new bands and only while the shear bands are growing. Furthermore, it achieves the added function of eliminating spurious band formation and accounting for the immediate effects of the new bands on the nearby cells.

The paper is organized as follows: first we describe the equations governing the deformation and the evolution of the shear band; then we describe the approximate Riemann solver, the difference scheme for hyperbolic regions, and the tracking algorithm for shear bands. We finish with an example of the formation and evolution of a shear band.

2. EQUATIONS

We consider a model for antiplane shearing that was proposed by Schaeffer [13] to study the formation of shear bands in granular materials. The fundamental variables are the Cauchy stress and the velocity. In antiplane shearing the deformation is homogeneous in the direction of motion. We fix this direction to be that of the z-axis. Then the velocity and stress will depend only on two dimensions of space $\mathbf{x} = (x_1, x_2)$ and the time t. The velocity vector has only one non-trivial component v in the z-direction. The components of the Cauchy stress tensor relevant to the deformation are T_{31} and T_{32}. We define a dimensionless stress vector $\boldsymbol{\tau} = (\tau_1, \tau_2)^T$ by identifying $\tau_1 = T_{31}$ and $\tau_2 = T_{32}$. These variables are subject to equations expressing the conservation of momentum

$$\partial_t v = c^2 \operatorname{div} \boldsymbol{\tau}, \tag{1}$$

where c is the speed of elastic waves. The constitutive relations take different forms for elastic and plastic deformations. We assume that the stress rate satisfies the equations of linear eleasticity during an elastic deformation,

$$\partial_t \boldsymbol{\tau} = \operatorname{grad} v, \tag{2}$$

while for plastic deformations the constitutive relations are expressed as

$$\left(I + \frac{1}{h(|\boldsymbol{\tau}|)} R\boldsymbol{\tau}\boldsymbol{\tau}^T\right) \partial_t \boldsymbol{\tau} = \operatorname{grad} v. \tag{3}$$

Here $h(|\boldsymbol{\tau}|)$ is the hardening modulus, which we assume satisfies $h' < 0$ and $h(1) = 0$. Also R is the rotation matrix $\left(\begin{smallmatrix}\cos\alpha & \sin\alpha \\ -\sin\alpha & \cos\alpha\end{smallmatrix}\right)$. The parameter α in the rotation matrix R characterizes the degree of non-associativity in the model.

The change from elastic to plastic behavior is described in terms of a yield condition of Von Mises type. For later use we define a measure of the accumulated stress as

$$\gamma(t, \mathbf{x}) = \max_{0 \le s \le t} (|\boldsymbol{\tau}(s, \mathbf{x})|). \tag{4}$$

We say that the material is deforming plastically if $\partial_t |\boldsymbol{\tau}(t, \mathbf{x})| > 0$ and $|\boldsymbol{\tau}(t, \mathbf{x})| = \max_{0 \le s \le t}(|\boldsymbol{\tau}(s, \mathbf{x})|)$; otherwise we say that the material is deforming elastically.

For the scope of this paper, instead of considering the deformation as governed by two alternative systems (1), (2) and (1), (3), we will combine both and express the resulting system as

$$\partial_t v = c^2 \operatorname{div} \boldsymbol{\tau} \tag{5a}$$

$$\partial_t \boldsymbol{\tau} = A(\boldsymbol{\tau}) \operatorname{grad} v \tag{5b}$$

where $A(\boldsymbol{\tau}) = I$ if the deformation is elastic and $A(\boldsymbol{\tau}) = I - (h + |\boldsymbol{\tau}|^2 \cos(\alpha))^{-1} R\boldsymbol{\tau}\boldsymbol{\tau}^T$ if the deformation is plastic.

We study the speed and structure of planar waves. For waves traveling in a fixed direction $\boldsymbol{\xi}$, the velocity and stress variables can be considered to depend only on time, and the space coordinate $\nu = \boldsymbol{\xi} \cdot \mathbf{x}$. In this case system (5) simplifies to

$$\partial_t \begin{pmatrix} v \\ \boldsymbol{\tau} \end{pmatrix} = \begin{pmatrix} 0 & c^2 \boldsymbol{\xi}^T \\ \mathbf{b} & 0 \end{pmatrix} \partial_\nu \begin{pmatrix} v \\ \boldsymbol{\tau} \end{pmatrix}, \tag{6}$$

where $\mathbf{b} = A(\boldsymbol{\tau}) \cdot \boldsymbol{\xi}$. The eigenvalues associated with this system are $\lambda = 0$ and $\lambda = \pm c\sqrt{\mathbf{b} \cdot \boldsymbol{\xi}}$, with corresponding eigenvectors (here $\boldsymbol{\xi}^\perp$ represents a vector orthogonal to $\boldsymbol{\xi}$)

$$\begin{pmatrix} 0 \\ \boldsymbol{\xi}^\perp \end{pmatrix}, \quad \begin{pmatrix} -\lambda \\ \mathbf{b} \end{pmatrix}. \tag{7}$$

A consequence of introducing non-associativity in the flow rule is the onset of ill-posedness in the sense of Hadamard; that is, there is a loss of hyperbolicity in system (6) whenever $\mathbf{b} \cdot \boldsymbol{\xi} < 0$. As it is shown in [13], for a given stress $\boldsymbol{\tau}$ hyperbolicity ($\mathbf{b} \cdot \boldsymbol{\xi} > 0$) is preserved for all directions $\boldsymbol{\xi}$ if and only if $h(|\boldsymbol{\tau}|) \ge |\boldsymbol{\tau}|^2 \sin^2(\alpha/2)$. From the properties of h, there is a unique γ_c such that $h(\gamma_c) = (\gamma_c)^2 \sin^2(\alpha/2)$ and hence a locus $|\boldsymbol{\tau}| = \gamma_c$ for which ill-posedness first occurs. For stress on that locus, $\boldsymbol{\tau} = \gamma_c(\cos\theta, \sin\theta)^T$, the direction $\boldsymbol{\xi}_c$ of the waves such that $\mathbf{b} \cdot \boldsymbol{\xi}_c = 0$ is the direction bisecting the angle made by $\boldsymbol{\tau}$ and $R\boldsymbol{\tau}$, that is $\boldsymbol{\xi}_c = (\cos(\theta - \alpha)/2, \sin(\theta - \alpha)/2)^T$. Following [13], we use ill-posedness as the criteria to introduce shear bands in the deformation.

2.1. *Shear Band*

The loss of hyperbolicity for system (5) is associated with the formation of shear bands. We idealize a shear band as a ''stationary'' discontinuity in a weak solution of (5). The shear band is stationary in the sense that once it occupies a location in the space plane, it will do so for the rest of the process; in that sense we would say that the discontinuity propagates with zero speed. This does not preclude the growth of the band as it extends at the endpoints. Schaeffer [13] proposes a description of the deformation at the shear band where the system is replaced by a set of jump discontinuities. For $\mathbf{n}$ the unit normal to the band, we express the stress in terms of a coordinate system aligned with the shear band: $\sigma = \boldsymbol{\tau} \cdot \mathbf{n}$ is the normal component of the stress and $\omega = \boldsymbol{\tau} \cdot \mathbf{n}^\perp$ is the transverse component. The constitutive assumptions are:

(i) the velocity is linear across the shear band and the velocity gradient (in a direction normal to the band) is approximated by an average jump, $\partial_{\mathbf{n}} v = [v]/\delta$, where $[v] = v_{\mathrm{br}} - v_{\mathrm{bl}}$ is the jump in the velocity across the band ($v_{\mathrm{bl}}, v_{\mathrm{br}}$ are the velocities at the left and right boundary of the shear band) and δ is a ''grain diameter'' parameter;

(ii) the normal component of the stress is continuous across the band;

(iii) inside the shear band, the transverse component ω jumps to a value larger than either of the one sided limits.

At the shear band, Eq. (5b) is replaced by a similar constitutive relation

$$\partial_t \begin{pmatrix} \sigma_b \\ \omega_b \end{pmatrix} = A(\sigma_b, \omega_b) \begin{pmatrix} [v]/\delta \\ 0 \end{pmatrix}, \tag{8}$$

and the supplementary relations relations describing the speed s of the shear band and continuity of σ_b,

$$s = 0, \quad [\sigma] = 0. \tag{9}$$

These jump conditions play a similar role to Rankine–Hugoniot conditions in gas dynamics, but we must note that, unlike Rankine–Hugoniot conditions, these jump conditions involve derivatives. We also point out that Eq. (8) provides the evolution of the stress inside the shear band. It is easy to check that during plastic loading $\partial_t \sigma < 0$ and therefore it is possible to match plastic loading inside

the shear band with elastic unloading outside the shear band.

2.2. *Eigenvalues and Eigenvectors*

System (5) is expressed in quasilinear form as

$$U_t + B_1 U_{x_1} + B_2 U_{x_1} = 0, \tag{10}$$

where

$$U = \begin{pmatrix} v \\ \tau_1 \\ \tau_2 \end{pmatrix}, \quad B_1 = \begin{pmatrix} 0 & c^2 & 0 \\ b_{11} & 0 & 0 \\ b_{21} & 0 & 0 \end{pmatrix}, \quad B_2 = \begin{pmatrix} 0 & 0 & c^2 \\ b_{12} & 0 & 0 \\ b_{22} & 0 & 0 \end{pmatrix}.$$

The coefficients b_{ij} take different values for elastic and plastic deformations: $b_{ij} = \delta_{ij}$ if the deformation is elastic and $b_{ij} = \delta_{ij} - (R\boldsymbol{\tau})_i \tau_j / (h + |\boldsymbol{\tau}|^2 \cos\alpha)$ if the deformation is plastic, where $R\boldsymbol{\tau} = \begin{pmatrix} \tau_1 \cos\alpha + \tau_2 \sin\alpha \\ -\tau_1 \sin\alpha + \tau_2 \cos\alpha \end{pmatrix}$. The corresponding eigenvalue and left eigenvector matrices for B_1 are

$$E_1 \equiv \begin{pmatrix} -c\sqrt{b_{11}} & 0 & 0 \\ 0 & 0 & 0 \\ 0 & 0 & c\sqrt{b_{11}} \end{pmatrix}, \; X_1 \equiv \begin{pmatrix} c\sqrt{b_{11}} & 0 & -c\sqrt{b_{11}} \\ b_{11} & 0 & b_{11} \\ b_{21} & 1 & b_{21} \end{pmatrix},$$

and similarly for B_2

$$E_2 \equiv \begin{pmatrix} -c\sqrt{b_{22}} & 0 & 0 \\ 0 & 0 & 0 \\ 0 & 0 & c\sqrt{b_{22}} \end{pmatrix}, \; X_2 \equiv \begin{pmatrix} c\sqrt{b_{22}} & 0 & -c\sqrt{b_{22}} \\ b_{12} & 0 & b_{12} \\ b_{22} & 1 & b_{22} \end{pmatrix}.$$

These relations show that the system is hyperbolic if $b_{ii} > 0$. We will also make use of these matrices in developing our numerical method.

3. RIEMANN SOLVER

The difference scheme described in Section 5 relies on approximate solutions to Riemann problems in one dimension. In what follows we will describe the solution to Riemann problems in the x_1-direction and an algorithm for the approximate solution to such initial value problem.

As in Section 2, setting $\xi = (1, 0)$, the characteristic speeds of waves in the x_1 direction are $\pm c$ for elastic waves and $\pm c_p$ for plastic waves, where $c_p = c\sqrt{b_{11}}$. While $c_p \leq c$, the wave structure of the solution to the Riemann problem has a simple description as two packets of waves, each containing two waves: a linear elastic wave that places the stress at most on the yield curve, followed by a plastic rarefaction continuing from there (see [6, 11]). Before we proceed to give a more detailed description we should notice that non-associative flow rules may imply that for certain values of stress $c_p > c$. In this model, this is the case for values of the stress (in the second and fourth quadrants) that satisfy $\tau_2/\tau_1 < \tan(\alpha + \pi/2)$. This phenomena has been pointed out in different contexts (see, for example, [9, 12, 14]) as a feature and difficulty on non-associative flow rule models. In the scope of this paper we exclude plastic shocks and therefore limit the region of existence for the solutions described by the numerical examples. In the computations presented in this paper, we check that the solution remains in the region where the solution to Riemann problems exist and do not include shocks (this is $c_p \leq c$). Existence of solutions of the Riemann problem for all data and possible modifications to the model are discussed in [5]. These modifications will change the model in order to assure that $c_p \leq c$ for all values of stress while retaining the regions of ill-posedness that imply the formation of shear bands.

In what follows we assume that $c_p \leq c$ and study the solution to Riemann problems. These solutions are described by means of the wave curves. For each wave packet, the wave curve is the locus of all states behind the wave packet that can be connected via admissible waves to a given state ahead of the wave packet. Since shock waves are not present in this model, the wave curves are defined as the integral curves to the vector fields defined by the eigenvectors (7) of the system. We remark that these eigenvectors are not continuous on elastic–plastic transitions. This makes our definition of wave curves a slight generalization of that of rarefaction wave solutions for a general hyperbolic system (see [10, 16] for a detailed description). We start by justifying a particular parameterization of the wave curves. The projection of the wave curves, for both left and right moving waves, onto the stress plane is given by the solution curves of the system of two ordinary differential equations

$$\frac{d\boldsymbol{\tau}}{ds} = \begin{pmatrix} b_{11}(\boldsymbol{\tau}) \\ b_{21}(\boldsymbol{\tau}) \end{pmatrix}. \tag{11}$$

As shown in [13], these solution curves are symmetric with respect to the origin (see Fig. 1) and approach an attractor A (resp. F, by symmetry) in the first (resp. third) quadrant. The curves ABC and DEF represent the locii of the values of stress satisfying $b_{11} = 0$ and the critical value of stress γ_c is the length of the stress vector $\boldsymbol{\tau}$ at either E of B (in Fig. 1 we assume that the stress has been rescaled as to satisfy $|\boldsymbol{\tau}| \leq 1$, as in [13]). The (projection of the) wave curves (12) will intersect the curves ABC (resp. DEF) at some point where $\tau_1 = \tau_1^M$ (resp τ_1^m).

In a purely one-dimensional model, those points of intersection would correspond to shear band initialization,

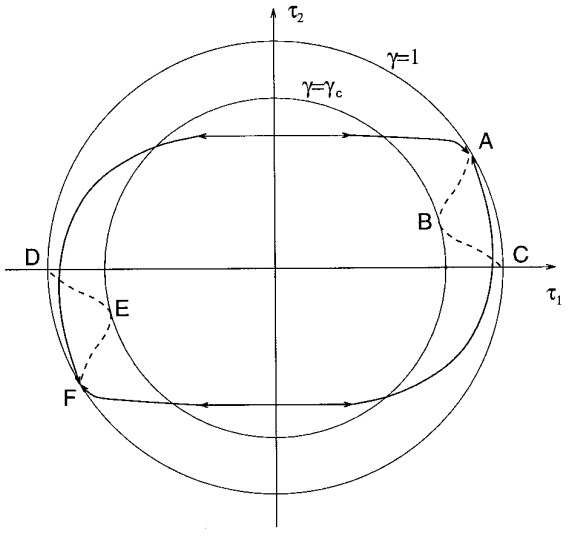

FIG. 1. Wave curves in a stress plane.

while in the present two-dimensional model those points are beyond the circle $|\boldsymbol{\tau}| = \gamma_c$ of ill-posedness. This permits us to study the wave curves when the τ_1 component of the stress is contrained to satisfy $\tau_1^m < \tau_1 < \tau_1^M$ and therefore a parameterization with respect to τ_1 is admissible.

We construct our Rieman problem solution as follows: Given an initial state

$$U^0 = \begin{pmatrix} v^0 \\ \tau_1^0 \\ \tau_2^0 \end{pmatrix}$$

with total stress γ^0, we define $\tau_1^e = \sqrt{(\gamma^0)^2 - (\tau_2^0)^2}$ as the elastic limiting value of τ_1. That is, a stress of the form $\boldsymbol{\tau} = (\tau_1, \tau_2^0)$ is inside the yield curve (and the corresponding deformation is elastic) if and only if $|\tau_1| \le \tau_1^e$. The (left moving) wave curves passing through U^0 are parameterized by τ_1 as

$$\begin{aligned} \mathsf{W}^{\mathrm{L}}(s, U^0) &= \begin{pmatrix} v(s, U^0) \\ \tau_1(s, U^0) \\ \tau_2(s, U^0) \end{pmatrix} \\ &= \begin{pmatrix} v^0 + \int_{\tau_1^0}^{s} c\{\sqrt{b_{11}(\eta, \tau_2)}\}^{-1}\, d\eta \\ s \\ \tau_2^0 + \int_{\tau_1^0}^{s} b_{21}(\eta, \tau_2)\, d\eta \end{pmatrix} \end{aligned} \tag{12}$$

for $\tau_1^m \le s \le \tau_1^M$ (the reader can consult Trangenstain and Pember [19] for a discussion of the derivation of the formula for plasticity). The total stress satisfies $\gamma(s, U^0) = \gamma^0$ for $|s| \le \tau_1^e$ and $\gamma(s, \mathrm{U}^0) = |\boldsymbol{\tau}(s, U^0)|$ for $|s| > \tau_1^e$. We notice that for $|s| \le \tau_1^e$ the stress satisfies $|\boldsymbol{\tau}(s, U^0)| < \gamma(s, U^0)$; that is, the wave curves are elastic, $b_{11} = 1$, and $b_{21} = 0$.

Similarly, the right moving wave curves are parameterized as

$$\begin{aligned} \mathsf{W}^{\mathrm{R}}(s, U^0) &= \begin{pmatrix} v(s, U^0) \\ \tau_1(s, U^0) \\ \tau_2(s, U^0) \end{pmatrix} \\ &= \begin{pmatrix} v_0 - \int_{\tau_1^0}^{s} c\{\sqrt{b_{11}(\eta, \tau_2)}\}^{-1}\, d\eta \\ s \\ \tau_2^0 + \int_{\tau_1^0}^{s} b_{21}(\eta, \tau_2)\, d\eta \end{pmatrix}. \end{aligned} \tag{13}$$

A solution to the Riemann problem with left and right states U^{L} and U^{R} is given by the intersection of the projections of the wave curves $\mathsf{W}^{\mathrm{L}}(s, U^{\mathrm{L}})$ and $\mathsf{W}^{\mathrm{R}}(s, U^{\mathrm{R}})$ onto the $v - \tau_1$ plane.

Since the wave curves W^{L} and W^{R} are bounded, it is possible that such an intersection does not exist (see [4, 6]). For these left and right states, the solution to the initial value problem is not self-similar and includes a shear band (with the corresponding relief fronts) connecting the traditional elasto-plastic waves (see [4, 6, 11]).

For the purpose of Section 5 we need to develop an approximate Riemann solver. We approximate the wave curves by piecewise linear curves. Since the portion of the wave curves corresponding to elastic deformations is linear, we retain this portion while we linearize the piece of the wave curve that corresponds to a plastic deformation. This linearization is made about the first point of intersection of the wave curve with the yield curve; this is $\boldsymbol{\tau} = (\pm\tau_1^e, \tau_2^0)$. The v and τ_2 components of the approximate wave curves $\mathsf{AW}^{\mathrm{L}}(\tau_1, U^0)$ for left moving waves are expressed as

$$v = v^0 + \psi_v(\tau_1, \tau_1^0, \tau_2^0, \tau_1^e) \tag{14}$$

$$\tau_2 = \tau_2^0 + \psi_{\tau_2}(\tau_1, \tau_1^0, \tau_2^0, \tau_1^e) \tag{15}$$

and similarly for the right moving waves $\mathsf{AW}^{\mathrm{R}}(\tau_1, U^0)$:

$$v = v^0 - \psi_v(\tau_1, \tau_1^0, \tau_2^0, \tau_1^e) \tag{16}$$

$$\tau_2 = \tau_2^0 + \psi_{\tau_2}(\tau_1, \tau_1^0, \tau_2^0, \tau_1^e). \tag{17}$$

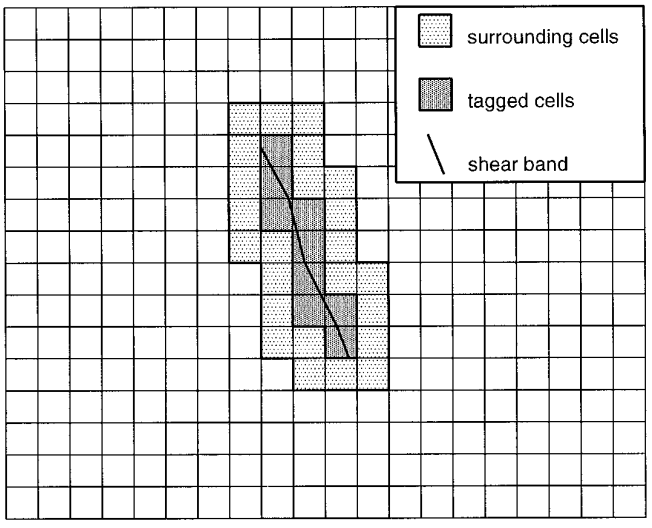

FIG. 2. Grid and shear band.

Here the functions ψ_v and ψ_{τ_2} are defined as

$$\psi_v(\tau_1, \tau_1^0, \tau_2^0, \tau_1^e) = \begin{cases} c(-\tau_1^e - \tau_1^0) + c(\tau_1 + \tau_1^e)/\sqrt{b_{11}(-\tau_1^e, \tau_2^0)} & \text{if } \tau_1 < -\tau_1^e, \\ c(\tau_1 - \tau_1^0) & \text{if } -\tau_1^e \le \tau_1 \le \tau_1^e, \\ c(\tau_1^e - \tau_1^0) + c(\tau_1 - \tau_1^e)/\sqrt{b_{11}(\tau_1^e, \tau_2^0)} & \text{if } \tau_1 > \tau_1^e, \end{cases} \tag{18}$$

$$\psi_{\tau_2}(\tau_1, \tau_1^0, \tau_2^0, \tau_1^e) = \begin{cases} b_{21}(-\tau_1^e, \tau_2^0)\,(\tau_1 + \tau_1^e) & \text{if } \tau_1 < -\tau_1^e, \\ 0 & \text{if } -\tau_1^e \le \tau_1 \le \tau_1^e, \\ b_{21}(\tau_1^e, \tau_2^0)\,(\tau_1 - \tau_1^e) & \text{if } \tau_1 > \tau_1^e. \end{cases} \tag{19}$$

We define the approximate Riemann solver operator $\mathsf{RP}(U^{\mathrm{L}}, U^{\mathrm{R}})$ which for a pair of left and right states, U^{L} and U^{R}, assigns the state defined by the intersection of the projections of the piecewise linear curves $\mathsf{AW}^{\mathrm{L}}(s, U^{\mathrm{L}})$ and $\mathsf{AW}^{\mathrm{R}}(s, U^{\mathrm{R}})$ onto the $v\tau_1$-plane.

4. OVERALL DESCRIPTION OF THE ALGORITHM

The numerical algorithm is best described as a superposition of two complementary algorithms: one dealing with the regions of the granular material where the deformation is continuous (no shear band present) and the other dealing with regions of the material where discontinuities (shear bands) occur.

We define a basic rectangular grid (we will refer to it as the hyperbolic grid) and tag all those cells traversed by a shear band (see Fig. 2). On this hyperbolic grid we superimpose an interface structure which comprises all the shear bands (tagged cells) and the surrounding cells. The data for the hyperbolic grid is associated with the center of the cells. Clearly, at the tagged cells, this data will be inaccurate since the hyperbolic grid ignores the presence of the shear bands. On the tagged cells, the data for the interface structure is associated to the subcells at both sides of the band and to the band itself (a more detailed description will be given in later sections). The cell-centered states of the hyperbolic grid are updated using a difference scheme of second-order accuracy. This process will give an incorrect result at the tagged cells (wrong data) and likely at the surrounding cells too. The latter is the case for several reasons: (i) the fluxes at boundaries of tagged cells are computed as solutions of Riemann problems with incorrect data coming from inside of the tagged cell, (ii) second order algorithms use the data of neighboring cells (including the tagged cells) for calculation of the slopes; and (iii) the tracking algorithm produces ''extra'' mass from the cells affected by the tracked front (tagged cells) that needs to be redistributed onto the neighboring cells.

Thus the algorithm for the updating of cell states is organized in two loops: (i) first we perform a loop over the whole hyperbolic grid where the cell-centered states are updated at each cell in the grid using the difference scheme described in Section 5; (ii) next we correct the data in all the tagged cells (traversed by the shear bands) and their surrounding cells as described in Section 6. Finally, when an updated state has the stress crossing the locus of ill-posedness ($|\boldsymbol{\tau}| = \gamma_c$), we incorporate that cell (the cell is tagged) into the interface structure. In Section 6.2 we describe this process in detail.

5. DIFFERENCE SCHEME

We now describe a numerical algorithm for the integration of the equations

$$v_t = c^2(\tau_1)_{x_1} + c^2(\tau_2)_{x_2}, \tag{20}$$

$$\boldsymbol{\tau}_t = A(\boldsymbol{\tau}) \begin{pmatrix} v_{x_1} \\ v_{x_2} \end{pmatrix}, \tag{21}$$

where the state U_{ij}^n is the average of $U = (v, \tau_1, \tau_2)^{\mathrm{T}}$ in the cell $[(i - \frac{1}{2})\Delta x_1, (i + \frac{1}{2})\Delta x_1] \times [(j - \frac{1}{2})\Delta x_2, (j + \frac{1}{2})\Delta x_2]$ at time $t_n = n\Delta t$. The superindex $n + \frac{1}{2}$ indicates that the state is evaluated at an intermediate time $t = t_n + \Delta t/2$, and the subindex $(i + \frac{1}{2}, j)$ corresponds to variables evaluated at the spatial point $(x_1, x_2) = ([i + \frac{1}{2}]\Delta x_1, j\Delta x_2)$. The state $U_{i+1/2,j}^{n+1/2}$ is taken to be the average value of U on the space time rectangle defined by $x_1 = [i + \frac{1}{2}]\Delta x_1$, $[j - \frac{1}{2}]\Delta x_2 < x_2 < [j + \frac{1}{2}]\Delta x_2$, $t_n < t < t_n + \Delta t$ (see Fig. 3). $U_{i,j+1/2}^{n+1/2}$ is defined similarly.

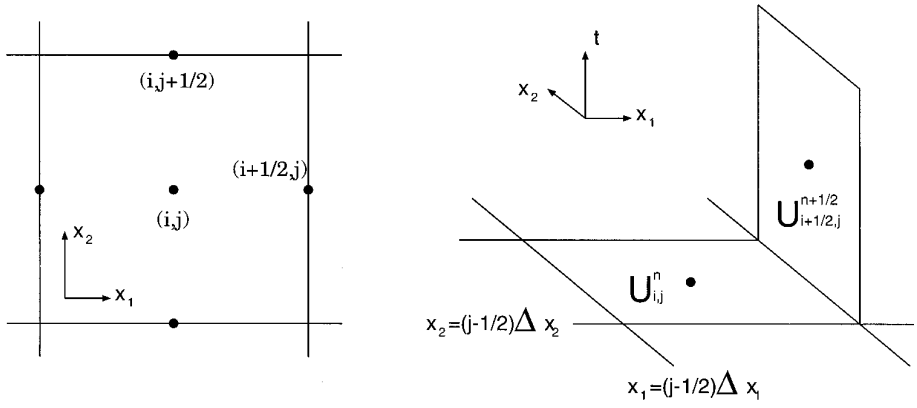

FIG. 3. States associated to the grid.

The equation for the conservation of momentum (20) can be integrated with a conservative difference

$$v_{ij}^{n+1} = v_{ij}^{n} + \frac{\Delta t}{\Delta x_1}\{(\tau_1)_{i+1/2,j}^{n+1/2} - (\tau_1)_{i-1/2,j}^{n+1/2}\} + \frac{\Delta t}{\Delta x_2}\{(\tau_2)_{i,j+1/2}^{n+1/2} - (\tau_2)_{i,j-1/2}^{n+1/2}\}. \tag{22}$$

The equation for the constitutive relations (21) is not in conservation form during plastic deformations. We will integrate them along a particle path [18]. Since there is no motion on the x_1x_2-plane, the particle path is a line with constant x_1 and x_2 coordinates, namely an ordinary differential equation:

$$\partial_t \boldsymbol{\tau} = A(\boldsymbol{\tau}) \begin{pmatrix} (v_{i+1/2,j}^{n+1/2} - v_{i-1/2,j}^{n+1/2})/\Delta x_1 \\ (v_{i,j+1/2}^{n+1/2} - v_{i,j-1/2}^{n+1/2})/\Delta x_2 \end{pmatrix}. \tag{23}$$

We notice that if the deformation is elastic, the integration of (23) takes a form similar to (22)

$$\boldsymbol{\tau}_{ij}^{n+1} = \boldsymbol{\tau}_{ij}^{n} + \frac{\Delta t}{\Delta x_1}\begin{pmatrix} v_{i+1/2,j}^{n+1/2} - v_{i-1/2,j}^{n+1/2} \\ 0 \end{pmatrix} + \frac{\Delta t}{\Delta x_2}\begin{pmatrix} 0 \\ v_{i,j+1/2}^{n+1/2} - v_{i,j-1/2}^{n+1/2} \end{pmatrix}. \tag{24}$$

The values $v_{i+1/2,j}^{n+1/2}$ and $v_{i-1/2,j}^{n+1/2}$, and similarly for $\boldsymbol{\tau}$, correspond to velocity and stress at the cell boundaries for an intermediate time $t = t_n + \Delta t/2$. These values are obtained as solutions to Riemann problems for appropriate left and right states which will be described below.

The scheme described above is based on the donor cell upwind scheme [3, 17, 18]. The calculation of the "flux" states $U_{i+1/2,j}^{n+1/2}$, $U_{i,j+1/2}^{n+1/2}$ is organized as follows: (i) calculation of predicted states to the left the right of the cell boundaries, $\tilde{U}_{i+1/2,j}^{n+1/2,\mathrm{S}}$ and $\tilde{U}_{i,j+1/2}^{n+1/2,\mathrm{S}}$ for S = L and R, via a characteristic tracing algorithm designed to provide second-order accuracy. Then predicted states at the boundaries are evaluated as solutions to Riemann problems. (ii) Correction of the predicted left and right states at the boundaries in the x_1 direction by taking into account the effect of transverse flow. The predicted states at the boundaries in the x_2 direction provide such correction. We do similar steps for the x_2 boundaries.

We will show in detail this process for cell boundaries parallel to the x_2-axis. A similar calculation provides the states at the cell boundaries parallel to the x_1-axis.

The calculation of $U_{i+1/2,j}^{n+1/2,\mathrm{L}}$ and $U_{i+1/2,j}^{n+1/2,\mathrm{R}}$ is based on a Taylor expansion of $U(x_1 + \Delta x_1/2, x_2, t + \Delta t/2)$ where we have used Eq. (10) to solve U_t in terms of U_{x_i}'s:

$$U\left(x_1 \pm \frac{\Delta x_1}{2}, x_2, t + \frac{\Delta t}{2}\right) \approx U(x_1, x_2, t) + \frac{1}{2}\left(\pm I - B_1 \frac{\Delta t}{\Delta x_1}\right)\Delta x_1 \left(\frac{\partial U}{\partial x_1}\right)_{ij} - \frac{\Delta t}{2} B_2 \left(\frac{\partial U}{\partial x_2}\right)_{ij}. \tag{25}$$

This calculation is performed in two steps in a "predictor–corrector" fashion. First we calculate the predicted values $\tilde{U}_{i+1/2,j}^{n+1/2,\mathrm{L}}$ and $\tilde{U}_{i-1/2,j}^{n+1/2,\mathrm{R}}$ for the simplified equation obtained by dropping from Eq. (25) the terms that include x_2 derivatives (that is, $(\Delta t/2)\ B_2\ (\partial U/\partial x_2)_{ij}$),

$$U(x_1 \pm \Delta x_1/2, x_2, t + \Delta t/2) \approx U(x_1, x_2, t) + \frac{1}{2}\left(\pm I - B_1 \frac{\Delta t}{\Delta x_1}\right)\Delta x_1 \left(\frac{\partial U}{\partial x_1}\right)_{ij}. \tag{26}$$

In this equation the variable x_2 is constant and therefore

we may consider the problem (and only at this step) of calculating of the predicted values $\tilde{U}^{n+1/2,\mathrm{L}}_{i+1/2,j}$ and $\tilde{U}^{n+1/2,\mathrm{R}}_{i-1/2,j}$ as purely one-dimensional. These predicted values are later corrected by incorporating the transverse flow effects of the $(\Delta t/2)\ B_2\ (\partial U/\partial x_2)_{ij}$ terms. The final (and corrected) values $U^{n+1/2,\mathrm{L}}_{i+1/2,j}$ and $U^{n+1/2,\mathrm{R}}_{i+1/2,j}$ have been obtained via a two-dimensional algorithm and satisfy the same stability properties as the one-dimensional problem (that is, the CFL number is 1).

5.1. CHARACTERISTIC TRACING

We describe the calculation of the predicted values of the states at the cell boundaries. A first step is the calculation of the gradient term $(\partial U/\partial x_1)_{ij}$, an approximation of $\partial U/\partial x_1$ in the ij-cell. This is done via a slope limiter algorithm that guarantees second-order accuracy and eliminates artificial oscillations [20]. We write $(\partial U/\partial x_1)_{ij} = \mathbf{muscl}(U^n_{i+1,j} - U^n_{i,j},\ U^n_{i,j} - U^n_{i-1,j})$, where the function **muscl** is defined as (the operations are performed component-wise)

$$\mathbf{muscl}(a,b) \equiv \frac{\mathrm{sign}(a) + \mathrm{sign}(b)}{2} \min\left(2|a|, 2|b|, \frac{|a+b|}{2}\right).$$

We write

$$\Delta x_1 \left(\frac{\partial U}{\partial x_1}\right)_{ij} = \begin{pmatrix} [v]^1_{ij} \\ [\tau_1]^1_{ij} \\ [\tau_2]^1_{ij} \end{pmatrix}.$$

Next we use the matrix of left eigenvectors X_1 to decompose the last term of (26) into the basic waves ($B_1 = X_1 \mathrm{diag}(-c\sqrt{b_{11}},\ 0,\ c\sqrt{b_{11}}) X_1^{-1}$). Only those waves which travel toward the corresponding boundary (and therefore will affect the states there) are retained. We now write the predicted values of $U^{n+1/2,\mathrm{L}}_{i+1/2,j}$ and $U^{n+1/2,\mathrm{R}}_{i-1/2,j}$ as

$$\tilde{U}^{n+1/2,\mathrm{L}}_{i+1/2,j} = U^n_{ij} + \left(1 - c\sqrt{b_{11}}\,\frac{\Delta t}{\Delta x_1}\right) \begin{pmatrix} -c\sqrt{b_{11}} \\ b_{11} \\ b_{21} \end{pmatrix} \left(-\frac{[v]^1_{ij}}{c\sqrt{b_{11}}} + \frac{[\tau_1]^1_{ij}}{b_{11}}\right) \quad (27)$$

$$\tilde{U}^{n+1/2,\mathrm{R}}_{i-1/2,j} = U^n_{ij} - \left(1 - c\sqrt{b_{11}}\,\frac{\Delta t}{\Delta x_1}\right) \begin{pmatrix} c\sqrt{b_{11}} \\ b_{11} \\ b_{21} \end{pmatrix} \left(\frac{[v]^1_{ij}}{c\sqrt{b_{11}}} + \frac{[\tau_1]^1_{ij}}{b_{11}}\right). \quad (28)$$

Remark 1. We notice that during the calculation of $\tilde{U}^{n+1/2,\mathrm{L}}_{i+1/2,j}$ and $\tilde{U}^{n+1/2,\mathrm{R}}_{i-1/2,j}$, the stress may lie outside the region of validity. In such a case we will lower the order of the algorithm at such cells to first order; that is, we set $\tilde{U}^{n+1/2,\mathrm{L}}_{i+1/2,j} = U^n_{ij}$ and $\tilde{U}^{n+1/2,\mathrm{R}}_{i-1/2,j} = U^n_{i,j}$. This is necessary in order to remain inside the region of hyperbolicity during the resolution of the Riemann problems at the cell-boundaries. As a justification of this step we should notice that this situation will occur near the shear band or at those points where the shear band is about to be formed. In any case a drop in accuracy to first order is reasonable since that is the formal order of accuracy maintained at the tracked front.

From these predicted values of the left and right states we obtain a predicted value of U at the boundary as a solution to a Riemann problem, $\tilde{U}^{n+1/2}_{i+1/2,j} = \mathsf{RP}(\tilde{U}^{n+1/2,\mathrm{L}}_{i+1/2,j}, \tilde{U}^{n+1/2,\mathrm{R}}_{i+1/2,j})$. This solution is obtained as described in Section 3. A similar process is followed to obtain $\tilde{U}^{n+1/2}_{i,j+1/2}$.

5.2. *Transverse Correction*

In Eq. (26) we have ignored the effects of the flow in the x_2 direction when we dropped the x_2 terms of Eq. (25). We approximate $(\partial U/x_2)_{ij}$ by $(\tilde{U}^{n+1/2}_{i,j+1/2} - \tilde{U}^{n+1/2}_{i,j-1/2})/\Delta x_2$ and correct the predicted values $\tilde{U}^{n+1/2}_{i+1/2,j}$ and $\tilde{U}^{n+1/2}_{i-1/2,j}$:

$$U^{n+1/2,\mathrm{L}}_{i+1/2,j} = \tilde{U}^{n+1/2,\mathrm{L}}_{i+1/2,j} - \frac{1}{2}\Delta t B_2 \frac{\tilde{U}^{n+1/2}_{i,j+1/2} - \tilde{U}^{n+1/2}_{i,j-1/2}}{\Delta x_2} \quad (29)$$

$$U^{n+1/2,\mathrm{R}}_{i+1/2,j} = \tilde{U}^{n+1/2,\mathrm{R}}_{i+1/2,j} - \frac{1}{2}\Delta t B_2 \frac{\tilde{U}^{n+1/2}_{i+1,j+1/2} - \tilde{U}^{n+1/2}_{i+1,j-1/2}}{\Delta x_2}. \quad (30)$$

Finally, we obtain the states at the boundary cells $U^{n+1/2}_{i+1/2,j} = \mathsf{RP}(U^{n+1/2,\mathrm{L}}_{i+1/2,j}, U^{n+1/2,\mathrm{R}}_{i+1/2,j})$.

Remark 2. A difficulty in computations of elastic–plastic deformations is that during a one timestep update the initial stress may be elastic while the stress at the end of the timestep could be beyond the yield curve. This problem is traditionally solved either by correcting the stress with a backward projection that places the stress on the yield surface or by the use of differential algebraic equations where the yield condition is the algebraic constraint. In our case this difficulty is avoided, since the transition from elastic to plastic can be resolved during the integration of (23). We denote

$$(\Delta v)_{ij} = \begin{pmatrix} (v^{n+1/2}_{i+1/2,j} - v^{n+1/2}_{i-1/2,j})/\Delta x_1 \\ (v^{n+1/2}_{i,j+1/2} - v^{n+1/2}_{i,j-1/2})/\Delta x_2 \end{pmatrix}$$

and the auxiliary function $\phi(z) = \boldsymbol{\tau}^n_{ij} + z(\Delta v)_{ij}$. If the result of integrating (23) as an elastic deformation ($A = I$), $\phi(\Delta t)$, is beyond the yield surface, the integration of (23) is done

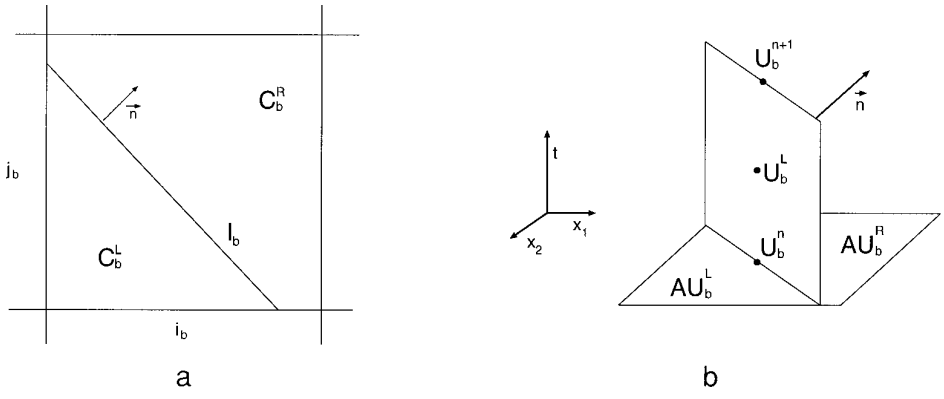

FIG. 4. States and regions associated to bonds.

in two steps: (i) We define $0 \le \Delta t^0 \le \Delta t$ as the intermediate time increment such that the stress given by $\phi(\Delta t^0)$ is at yield and integrate (23) up to Δt^0, while the deformation is elastic. (ii) We integrate (23), as a plastic deformation, for $t^n + \Delta t^0 \le t \le t^n + \Delta t$ with initial values $\boldsymbol{\tau}_{ij}(t^n + \Delta t^0) = \phi(\Delta t^0)$. This integration is done for the polar representation of the stress $\tau_1 = \gamma \cos\theta$ and $\tau_2 = \gamma \sin\theta$ and, since $|\boldsymbol{\tau}| = \gamma$, the stress is maintained at yield during the integration. The yield condition $\phi(\Delta t^0) = \gamma_{ij}^n$ provides a constraint equation for Δt^0, $|\boldsymbol{\tau}_{\mathrm{ij}}^n + z(\Delta v)_{ij}|^2 = (\gamma_{ij}^n)^2$, from which we compute Δt^0 explicitly. This is $\Delta t^0 = (-A + \sqrt{A^2 + BC})/C$, where $A = \boldsymbol{\tau}_{ij}^n \cdot (\Delta v)_{ij}$, $B = (\gamma_{ij}^n)^2 - |\tau_{ij}^n|^2$, and $C = |(\Delta v)_{ij}|^2$.

6. TRACKING OF THE SHEAR BAND

We now describe the tracking algorithm at the shear bands. From a computational point of view, the shear band is idealized to have infinitesimal width while the physical width is kept as a parameter δ in the equation of evolution of the band (8). With this idealization, the shear band will be constrained to be (width-wise) inside one cell. This will present no difficulties for the study of the overall effect of the shear band on the domain at large.

The shear band is approximated as an oriented piecewise linear curve in the **x** plane. The intersection of the band with a cell is a linear segment that divides the cell in two disjoint regions. That is, the shear band is not allowed to end in the interior of a cell. These segments are called bonds and the intersection of the shear band with grid lines are called points.

The approach used here follows traditional front tracking techniques [2, 8] with modifications proper to this problem: the tracked front is neither a hyperbolic wave nor does it divide the domain into unconnected domains. The tracking algorithm consists of two major blocks: (a) updating the states at and near the shear band and (b) initialization and growth of the shear band.

6.1. *Integration Algorithm near the Shear Band*

We denote by (i_b, j_b) the index of a generic tagged cell (intersected by a shear band). We refer to the cell as C_b and the bond (piece of the band in the C_b) as I_b. In the process of tracking the bond I_b we will need to access data of the states on the neighboring cells. We define an auxiliary box of indices, centered at (i_b, j_b), as $B = [i_b - 1, i_b + 1] \times [j_b - 1, j_b + 1]$, and the same box excluding the center as $B^o = B - (i_b, j_b)$. Since the shear band is an oriented curve, we can define a normal to the band, **n** and left and right sides to the band. The two disjoint regions in C_b separated by the band are referred as the left, C_b^{L}, and right, C_b^{R}, subcells (see Fig. 4a).

These subcells have states $AU^{\mathrm{L},n}$ and $AU^{\mathrm{R},n}$ associated with them at time $t = t_n$. Other states associated with the bond are:

— U_b^n, the state at the shear band at time $t = t_n$,

— U_b^{L} and U_b^{R}, the temporary states at the sides of the band at time $t = t_n + \Delta t/2$. These states are used to calculate the temporary flux-like quantities (v and $\boldsymbol{\tau}$ in the right-hand side of (20)–(21)) at the shear band.

We organize the description of the method as follows: (a) averaging states near the band, (b) updating the states at the band, (c) recalculation of fluxes at and near the band, (d) redistribution of excess numerical mass, and (e) integration on subcells and cells near the band.

Locally, for the cells surrounding the bond, we also define left and right states: for $(i, j) \in B$ and $S = \mathrm{L}, \mathrm{R}$; $U_{i,j}^S = AU_{i,j}^{S,n}$ if the shear band intersects the (i, j) cell and $U_{i,j}^S = U_{i,j}^n$ otherwise. For cells next to the tips of the bands, and only for the purpose of assigning left and right areas to these cells, we extrapolate the band at its endpoints by one or two cells in the direction of the last bond.

(a) *Averaging the states.* In what follows, we will refer to a left or right state with the index $S = \mathrm{L}, \mathrm{R}$. The area of the left and right subcells can be very small compared

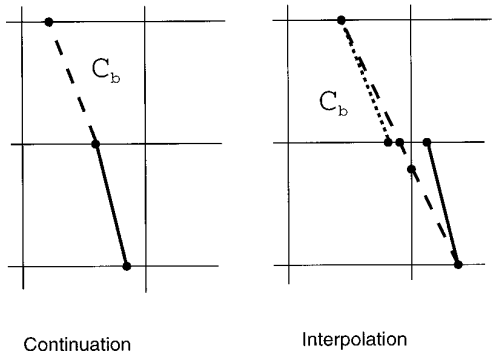

FIG. 5. Bond initialization.

to the area of a regular cell ($\Delta x_1 \Delta x_2$) and thus the states U^S associated to those regions would be suspect. We replace those states by a weighted average of the states associated to cells (or subcells) contiguous to C_b, for the corresponding side of the band. We use the following weighted interpolation:

$$AU^{S,n} = \frac{A^S_{i_b,j_b}}{\Delta x_1 \Delta x_2} U^S + \left(1 - \frac{A^S_{i_b,j_b}}{\Delta x_1 \Delta x_2}\right) \frac{\sum_{(i,j)\in B^o} A^S_{ij} U^S_{ij}}{\sum_{(i,j)\in B^o} A^S_{ij}},$$

where $A^S_{i,j}$ is the area of the portion of the cell $C_{i,j}$ to the S side of the band.

(b) *Updating the states at the band.* The evolution of the stress in the interior of the band is described in Section 2.1 by Eq. (8). There we defined σ and ω as the components of the stress in a coordinate system aligned with the shear band. We denote by σ^n_b, ω^n_b, γ^n_b the stress variables inside the band at $t = t_n$. The values of stress σ^{n+1}_b, ω^{n+1}_b, γ^{n+1}_b, at time $t_n + \Delta t$ are calculated by means of a numerical integration of (8), together with (4), from t_n to $t_n + \Delta t$ with initial data σ^n_b, ω^n_b, γ^n_b. The jump in velocity $[v]$ in (8) is approximated by $[v] = \tilde{v}^{\mathrm{R}}_b - \tilde{v}^{\mathrm{L}}_b$, where $\tilde{v}^S_b$ are the velocities of the states at the sides of the band at time t_n. These are the states connected to $AU^{S,n}$ by a pack of waves moving to the left ($S = L$) or to the right ($S = \mathrm{R}$). They are given by the solution to a Goursat–Riemann problem (similar to a Riemann problem but defined on a quarter plane with initial and boundary conditions) with initial values at $t = t_n$ determined by the side state $AU^{S,n}$ and the boundary condition imposed on the shear band, $\sigma = \sigma^n_b$. We calculate $\tilde{v}^S_b$ by tracing one parameter (approximated) wave curves AW^S. We write the stress components in $AU^{S,n}$ as σ^S_0, ω^S_0, and γ^S_0 and define the auxiliary quantity $\sigma^{S,e} = \sqrt{(\gamma^S_0)^2 - (\sigma^S_0)^2}$. Then

$$\tilde{v}^S_b = v^S_0 - (-1)^S \psi_v(\sigma^n_b, \sigma^S_0, \omega^S_0, \sigma^{S,e}), \tag{31}$$

where $(-1)^{\mathrm{L}} = -1$ and $(-1)^{\mathrm{R}} = 1$ and ψ_v is defined in (20).

(c) *Calculation of fluxes.* The next step is to calculate the states U^S_b at the sides of the band at $t = t_n + \Delta t/2$. These states will be used to calculate fluxes on the side of the shear band. As in (b), the states U^S_b obtained from the solution to a Goursat–Riemann problem, where this time the data on the shear band is the value of σ at $t = t_n + \Delta t/2$. We approximate this value by $\sigma^{n+1/2}_b = (\sigma^n_b + \sigma^{n+1}_b)/2$ and identify $\sigma^{\mathrm{R}}_b = \sigma^{\mathrm{L}}_b = \sigma^{n+1/2}_b$. The other components of U^S_b are given by

$$\tilde{v}^S_b = v^S_0 - (-1)^S \psi_v(\sigma^S_b, \sigma^S_0, \omega^S_0, \sigma^{S,e}) \tag{32}$$

$$\omega^S_b = \omega^S_0 + \psi_v(\sigma^S_b, \sigma^S_0, \omega^S_0, \sigma^{S,e}). \tag{33}$$

The states $U^{n+1/2}_{i+1/2,j}$ and $U^{n+1/2}_{i,j+1/2}$ were calculated in Section

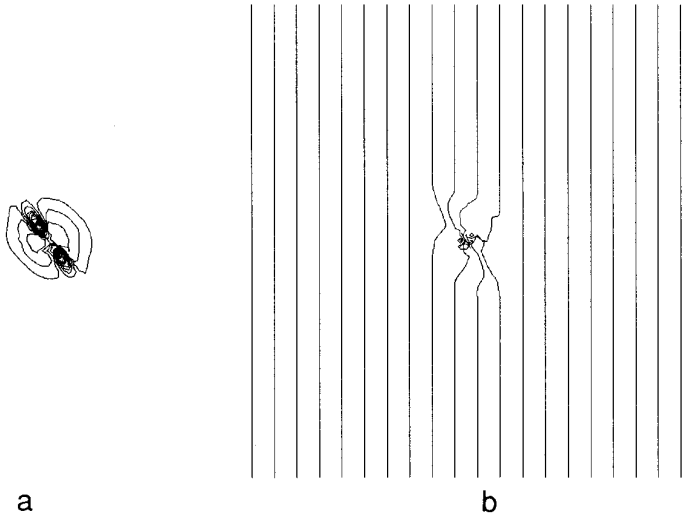

FIG. 6. γ and v contour lines at time $t = 0.0989$.

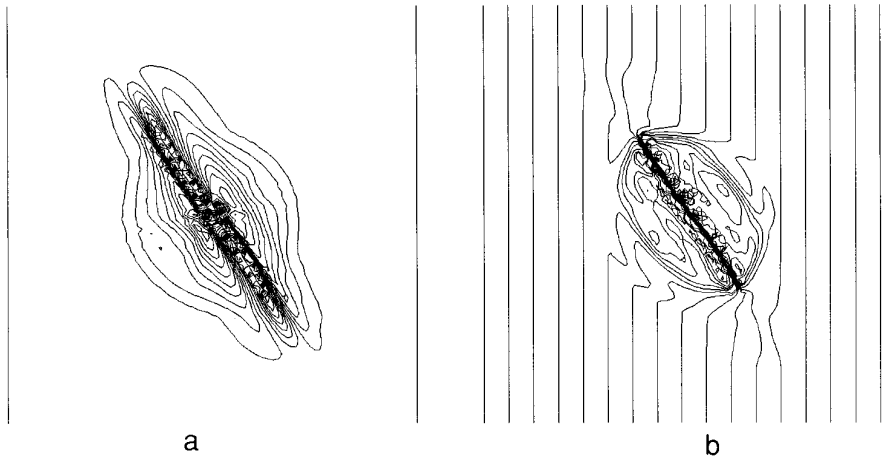

FIG. 7. γ and v contour lines at time $t = 0.3956$.

5, for cell edges in B, using incorrect data for the subcells of C_b. We proceed to recalculate these states, but this time we do it with first-order accuracy since that is the expected accuracy at the tracked front. The correct states are obtained as in Section 5, for the left and right sides of the band: $U^{S,n+1/2}_{i+1/2,j} = \mathsf{RP}(U^{S,n}_{i,j}, U^{S,n}_{i+1,j})$ and $U^{S,n+1/2}_{i,j+1/2} = \mathsf{RP}(U^{S,n}_{i,j}, U^{S,n}_{i,j+1})$. During the recomputation of the fluxes on cell edges adjacent to the shear band, the transverse corrections are not ignored. The stress vector on the band is expressed in terms of the components in the grid directions and (29)–(30) are still valid.

(d) *Redistribution of numerical mass.* For each cell edge in the box B we have assigned a state for the portion of the edge on each side of the shear band. We denote by $d^S_{i+1/2,j}$ (resp. $d^S_{i,j+1/2}$) the length of the bond segment. For the irregular cell C^S_b, the momentum equation is integrated to

$$\begin{aligned} A^S_{i_b,j_b}[(v^S)^{n+1}_{i_b,j_b} - (v^S)^n_{i_b,j_b}] = \Delta t[&d^S_{i_b-1/2,j_b}(\tau^S_1)^{n+1/2}_{i_b-1/2,j_b} \\ &- d^S_{i_b+1/2,j_b}(\tau^S_1)^{n+1/2}_{i_b+1/2,j_b} + d^S_{i_b,j_b-1/2}(\tau^S_2)^{n+1/2}_{i_b,j_b-1/2} \\ &- d^S_{i_b,j_b+1/2}(\tau^S_2)^{n+1/2}_{i_b,j_b+1/2} + (-1)^S d_b \sigma^S_b], \end{aligned} \tag{34}$$

where $(-1)^{\mathrm{L}} = -1$ and $(-1)^{\mathrm{R}} = 1$.

If we write M^S_b for the RHS of (34) and $M_{i,j}$ as the corresponding quantity in (22), we would like to write

$$(v^S)^{n+1}_{i_b,j_b} = (v^S)^n_{i_b,j_b} + \frac{M^S_b}{A^S_{i_b,j_b}}. \tag{35}$$

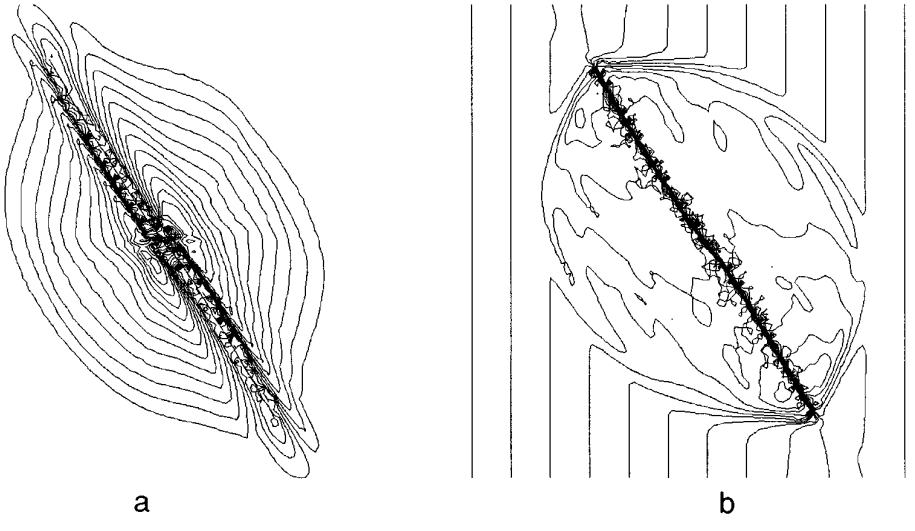

FIG. 8. γ and v contour lines at time $t = 0.5934$.

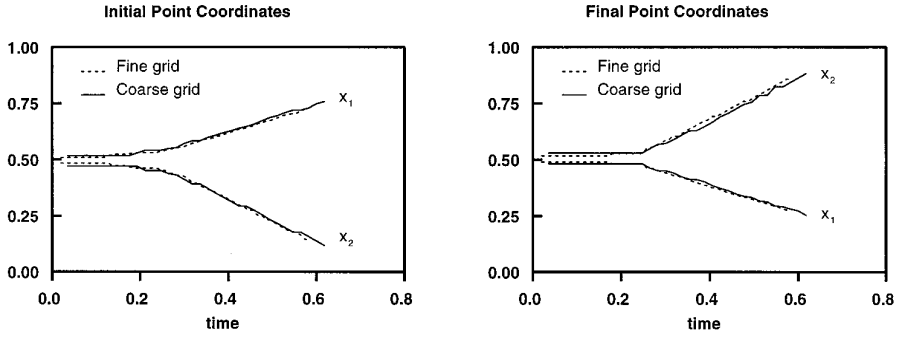

FIG. 9. Location of endpoints of shear band.

But, if $A^S_{i_b,j_b}$ is too small, (35) would violate the CFL stability condition. Instead, we write

$$(v^S)^{n+1}_{i_b,j_b} = (v^S)^n_{i_b,j_b} + \frac{M^S_b}{\Delta x\,\Delta y}. \tag{36}$$

This expression for $(v^S)^{n+1}_{i_b,j_b}$ satisfies the CFL condition, but when we compute the integral of the momentum equation in the region $C^S_b \times [t_n, t_n + \Delta t]$ and compare with (34) we observe that there is an excess of mass flux that is given by

$$M^S_b - A^S_{i_b,j_b}((v^S)^{n+1}_{i_b,j_b} - (v^S)^n_{i_b,j_b}) = M^S_b\left(1 - \frac{A^S_{i_b,j_b}}{\Delta x\,\Delta y}\right). \tag{37}$$

In order to be conservative in the region, we need to put the above excess "mass-flux" back into the algorithm. There are several techniques to carry out this mass redistribution. We partially follow the ideas of [2], in the sense that we perform a weighted area redistribution, with some variations. The fact that the front is not hyperbolic precludes a wave decomposition at the front, and the fact that the material presents a sharp discontinuity in the displacement indicates that transfer of "mass-flux" across the discontinuity is not proper. The excess numerical mass is distributed over all the cells surrounding the bond, with each cell receiving a contribution to the numerical mass in (22) or (34) of $M^S_b(1 - A^S_{i_b,j_b}/\Delta x\,\Delta y)/\Sigma_{(m,n)\in B^o} A^S_{m,n}$.

(e) *Integration near the band.* Once the mass redistribution has been performed for each bond of each shear band, we update the cells affected by the shear bands. If the cell (i, j) is in a box B for some bond of a shear band, we recompute the velocity at the new level ($t = t_{n+1}$), including the redistributed mass contributed by all bonds over all shear bands: if the shear band does not intersect $C_{i,j}$,

$$v^{n+1}_{i,j} = v^n_{i,j} + \frac{M_{i,j}}{\Delta x\,\Delta y} + \sum_S \sum_F \left(M^S_b\left((1 - \frac{A^S_{i_b,j_b}}{\Delta x\,\Delta y}\right)\frac{1}{\Sigma_{(m,n)\in B^o} A^S_{m,n}}\right) \tag{38}$$

and, otherwise,

$$(v^S)^{n+1}_{i,j} = (v^S)^n_{i,j} + \frac{M^S_{i,j}}{\Delta x\,\Delta y} + \sum_F \left(M^S_b\left(\left(1 - \frac{A^S_{i_b,j_b}}{\Delta x\,\Delta y}\right)\frac{1}{\Sigma_{(m,n)\in B^o} A^S_{m,n}}\right)\right). \tag{39}$$

The sum Σ_F is over all the band bonds that affect the (i, j) cell. A similar process is done for the stress update.

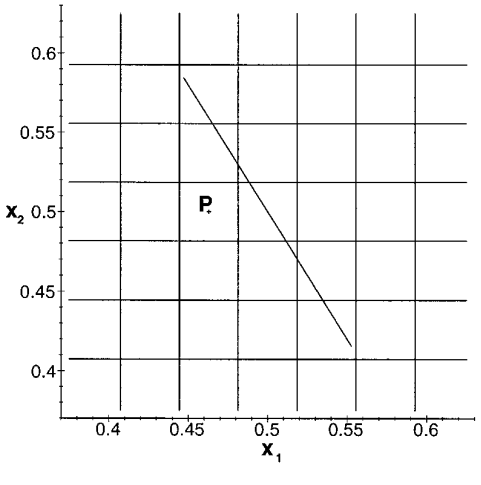

FIG. 10. Location of initial shear band and test point on coarse grid.

6.2. *Initialization of the Shear Band Cell*

As mentioned in Section 2, system (5) becomes ill-posed, in the sense of Hadamard, when the total stress γ reaches a critical value γ_c. This ill-posedness is used as a criterion for the formation (or extension) of shear bands. If γ reaches

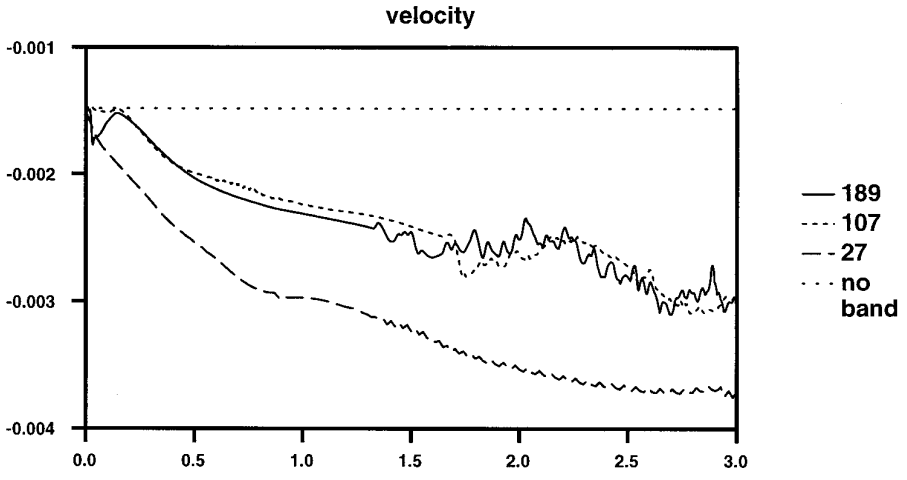

FIG. 11. Velocity as function of t at $\mathbf{P}(0.462963, 0.5)$.

the critical value γ_c, at a time t_0 in the cell C_b, then a shear band bond is placed in C_b, with orientation given by the direction of ill-posedness of system (5). That is, if θ is the argument of the stress vector in the cell C_b, the normal to the bond is given by $\mathbf{n} = (\cos((\theta - \alpha)/2), \sin((\theta - \alpha)/2))^T$. The exact placement of the bond in the cell is determined differently if the bond corresponds to an existing shear band growing into the cell or to the formation of an entirely new shear band. If the boundary of C_b contains the end-point P of a shear band, we place the new bond, with the given orientation, as to continue the existing shear band at P (see Fig. 5a). Otherwise, we locate a local maximum of $\gamma(t_0, x, y)$ in the cell C_b and place the bond as a segment of the straight line passing through the local maximum and with normal $\mathbf{n}$. It may occur that a shear band will end at one of the cells surrounding C_b but the end point is not on the boundary of C_b. In that case, after creating the new band, we check the orientation of the contiguous bands and, if the orientations are similar, we connect both bands via an interpolation process (see Fig. 5b).

The above process describes the formation of a new bond at exactly the onset of ill-posedness. In general we expect that at the end of a timestep, the stress at one or several cells could be beyond the locus of initial ill-posedness, $\gamma_{i,j}^{n+1} \geq \gamma_c$, while at the beginning of the timestep we had $\gamma_{i,j}^{n+1} < \gamma_c$. We would expect new shear band bonds to be created at some intermediate time according to the above description. Also those new bonds could be associated with different shear bands or one single band growing rapidly since there is no a priori limit in the rate of growth of the shear band. In order to accurately describe the evolution of the shear bands we perform a series of cell updates at partial timesteps in a way that at the end of each partial timestep, only one cell is allocated a new bond,

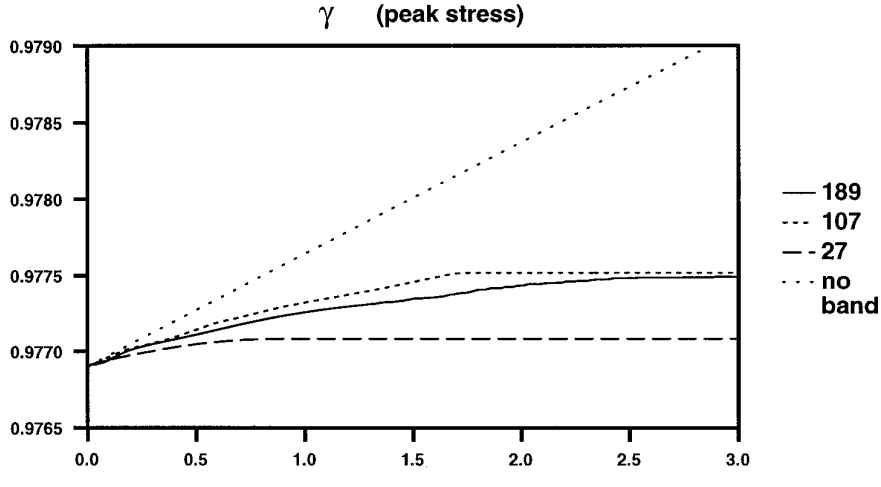

FIG. 12. γ as functions of t at $\mathbf{P}(0.462963, 0.5)$.

and this occurs at values of stress $\gamma = \gamma_c$. The process is described as follows: (a) After a regular time step $[t_n, t_n + \Delta t]$, we sweep over all the cells which were not intersected by shear bands at $t = t_n$. We tag those cells $C_1, ..., C_m$, where the stress has gone beyond the critical yield value $|\boldsymbol{\tau}| = \gamma_c$. If no such cells are found, we terminate the process. Otherwise (b) we write $\gamma(t, k)$ for the solution of (23) at each C_k in $[t_n, t_n + \Delta t]$ and for each k we find the first t_k such that $\gamma(t_k, k) = \gamma_c$. (c) We label $t^*_{k_b} = \min_{k=1,...m} t_k$ and integrate up to $t^*_{k_b}$ at the $\{C_k\}_{k=1}^m$ cells and also at the cells intersected by the shear bands. This will give us the first cell C_{k_b} in which to place a shear band as discussed above. With this procedure, all the cells that are relevant to calculations on the shear bands are updated in a consistent manner. Finally, we repeat the above process from time $t = t^*_{k_b}$, adding, if necessary, new cells to the collection of tagged cells until we exhaust the time interval. Although the process is potentially computationally intensive it is performed only during a small portion of the simulation. We remark that the subcycling with partial timesteps is only applied (a) to the cells intersected by shear bands and those potentially given rise to shear bands but (b) only while the shear bands are growing. For example, in the simple case of a single band across the domain, the above procedure affects only those cells on the band and cells directly ahead of the band tips, but only while the band is growing. Once the band reaches the boundaries of the domain, no more cells need to be tagged and this iterative process is not entered.

With this process we take into account the effect of newly formed shear bands on their neighboring cells, either by accelerating the loading rate (and possibly introducing new band cells) or by unloading the nearby cells (and eliminating extraneous shear bands).

7. EXAMPLES

The following example describes the deformation of a prestressed material under uniform loading. The initial data consists of constant stress and velocity on the x_2-directions and linear on the x_1-direction. For this initial data and a homogeneous sample (same material properties across the domain) the deformation would maintain the same profile at all times; that is, the stress would remain constant as a function of the space variables (but changing with time) and the velocity would be constant on time (see [13]). We introduce an inhomogeneity in a small region at the center of the domain, in effect lowering the threshold for ill-posedness in system (5) and assuring that the shear band will form first in this region.

The initial data in consideration consists of a stress with modulus $|\boldsymbol{\tau}_0| = 0.9766$ and an argument of 0.7 radians. The material is assumed to be at yield, that is, $\gamma_0 = |\boldsymbol{\tau}_0|$ and loading with an initial velocity $v_0(x_1, x_2) = 0.26(2x_1 - 1)$ for $0 < x_1, x_2 < 1$. The velocity is constant at the x_1 boundaries $v(t, 0, x_2) = -0.26$ and $v(t, 1, x_2) = 0.26$. At the x_2 boundaries, $x_2 = 0$ and $x_2 = 1$, we extend the data at the edge of the domain in a normal direction beyond the physical domain. We remark that the data is given without units since we are using a nondimensionalized model. We refer to the Appendix in [13] for a more detailed description. The material constants are $c = 1$ (elastic wave speed) and $h(\gamma) = 1 - \gamma$. The inhomogeneity of this example is introduced with α, the parameter that measures the degree of non-associativity in the material. We consider a constant value of $\alpha = 0.261$ across the domain except at the center and cells immediately above and below for which we set $\alpha = 0.315$. For this choice of parameters and initial data the system is initially well posed and the material is deforming plastically everywhere in the domain.

A shear band is formed at a short time after the initialization of the test. In Fig. 6 we show contour plots (a) for γ and (b) for v soon after the formation of the shear band. For a correct interpretation of the figures we remark that if the material were homogeneous, the γ plot would show no contours (γ would be constant) and the velocity plot would consist of a series of vertical lines (velocity would be constant on x_2 and linear on x_1).

The material continues to load driven by the gradient of $\mathbf{v}$ away from the band. We can observe already the unloading fronts that propagate orthogonally from the shear band as predicted in [15] and observed in previous calculations for the one-dimensional case [6, 11]. We also notice the increase in loading ahead of the endpoints of the band which will cause the growth of the band as observed in Figs. 7 and 8).

We study the orientation of the shear band. For the given initial stress $\boldsymbol{\tau}_0$ (with argument of 0.7 radians) and the non-associativity parameter α (0.261 radians), we expect that the shear band will grow with a normal direction of 0.5695 radians (angle that the normal vector makes with the x_1 axis). This first approximation is obtained by noticing that when a shear band is formed, its orientation is given by rotating stress (clockwise) the stress at that point by an angle $\alpha/2$. In this example we cannot predict the exact value of stress at the point of formation of the shear band, but since the material has been prestressed to a level close to the value of ill-posedness, we expect that the direction of the stress will not vary greatly from the initial direction. We take this initial direction as the orientation of the shear band and compare it with the numerical results. In the numerical example, the orientation of the shear band is approximately 0.5896 radians and differs from the predicted value by 0.02 radians.

An important issue in this work is the accuracy of the front tracking algorithm, including the strategy for moving the endpoints of the shear band. An accurate algorithm

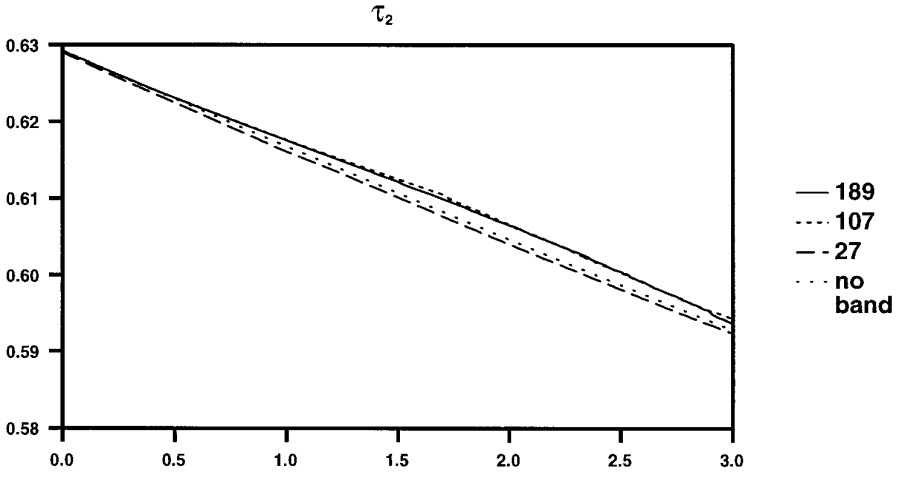

FIG. 13. τ_2 as function of t at **P**(0.462963, 0.5).

can help us discover how the speed of propagation of the shear band tip behaves. In Fig. 9 we compare the location of the endpoints of the shear band for two grids of different size (a coarse grid of 51 × 51 cells and a finer grid of 91 × 91 cells). Each graph shows the x_1 and x_2 coordinates of the initial point of the band and final point of the band, respectively, where the band is oriented in a direction of decreasing x_1 and increasing x_2. We observe that the location of the initial and final points is approximately the same for both grids.

As a concluding remark we point out that numerical algorithm described in this paper allows for computations where the growth of the shear band is greater than a cell per time step, the growth of the band is independent of the grid size and the orientation of the computed band accurately follows the predicted values.

8. A CONVERGENCE TEST

In this section we study the behavior of the solution near the tracked front. In order to allow for a longer period of loading we consider initial data with a smaller velocity gradient than in the previous example, $v_0(x_1, x_2) = 0.02(2x_1 - 1)$ for $0 < x_1, x_2 < 1$. We set the stress to a constant value of $|\boldsymbol{\tau}_0| = 0.9769$ and argument of 0.7 radians. Also, in order to minimize the initial effects of the tips of the shear band on the test point, we initialize a shear band of length 0.2 units at the center of the domain (see Fig. 10.) With this choice of data, the shear band does not change in length for a period of time. At $t \approx 1.3$, the band starts to grow at the tips.

We fix a point **P** with coordinates (0.462963, 0.5) on a cell (for the coarser grid) contiguous to the shear band (see Fig. 10). We analyze the behavior of the velocity v and of γ as functions of time at the point **P**. We compare these values for grids of different sizes (27 × 27, 107 × 107, and 189 × 189) with baseline values that correspond to the same material sample but homogeneous and without a shear band. A first observation is the decay of the velocity (Fig. 11) and the evolution of γ to a constant value (Fig. 12). These properties are predicted in the one dimensional case [15] in contrast with the case of a homogeneous sample without shear bands [13], where the velocity remains constant and γ grows steadily. A second observation is the convergence of the solution as the grid is refined. We observe oscillations that begin when the shear band begins to grow. We remark that the band represents a change in material properties, from hyperbolic to elliptic, as well as from continuum to particulate. As the shear band grows, the states on the new band cells undergo a fundamental change. In particular, they move from a regime of critical loading to one of elastic unloading. Acoustic waves are generated during this transition that propagate undamped along the shear band. These fluctuations are easier to observe in quantities that have a small variance in time, such as velocity (Fig. 11) and $|\boldsymbol{\tau}|$, but harder to observe on the components of the stress, τ_1 and τ_2, which have a larger variance (Fig. 13). We remark that some experiments by Behringer [1] indicate the existence of fluctuations in stress during shear with existing shear bands. These fluctuations are explained by the dynamics of the motion at a molecular scale. Our fluctuations are simply associated with the jump of the shear band tip across the next cell. Thus, although the fluctuations observed in this paper represent a reasonable qualitative behavior, we do not claim that they represent the correct physics.

A better study of convergence of the solution under grid refinement requires a choice of finer grids and falls out of the scope of this paper. As an ongoing project we are developing a code which combines the front tracking technique explained in this paper with an adaptive mesh re-

finement algorithm that focuses the computing effort in the regions near the shear band while allowing for larger cell elsewhere [7].

REFERENCES

1. R. Behringer, private communication, 1995.
2. I-L. Chern and P. Colella, Tech. Report UCRL-97258, Lawrence Livermore National Laboratory, Lawrence Livermore National Laboratory, Berkeley, CA 94720, July 1987 (unpublished).
3. P. Colella, *J. Comput. Phys.* **87,** 171 (1990).
4. X. Garaizar, *Q. Appl. Math.* **52,** 289 (1994).
5. X. Garaizar and M. Gordon, preprint, 1994.
6. X. Garaizar and D. Schaeffer, *J. Mech. Phys. Solids* **42**(1), 21 (1994).
7. X. Garaizar and J. Trangenstein, preprint, 1995.
8. J. Glimm, E. Isaacson, D. Marchesin, and O. McBryan, *Adv. Appl. Math.* **2,** 91 (1985).
9. M. Gordon and X. Garaizar, preprint, 1994.
10. P. D. Lax, *Commun. Pure Appl. Math.* **10,** 537 (1957).
11. D. G. Schaeffer, M. Shearer, F. X. Garaizar, and J. Trangenstein, "Numerical Computations for Shear Bands in an Antiplane Shear Model," in *Annual ARO Conference on Applied Mathematics and Computing,* Vol. ARO 94-1, 1994, p. 15.
12. I. Sandler and D. Rubin, "The Consequences of Non-associated Plasticity in Dynamic Problems," in *Constitutive Laws for Engineering Materials: Theory and Applications* edited by C. S. Desai *et al.* (Elsevier, New York, 1987), p. 345.
13. D. G. Schaeffer, *Proc. R. Soc. London* **436,** 217 (1992).
14. D. G. Schaeffer and M. Shearer, *European J. Appl. Math.* **3,** 225 (1992).
15. M. Shearer and D. G. Schaeffer, *Q. Appl. Math.* **52**(3), 579 (1994).
16. J. Smoller, *Shock-Waves and Reaction-Diffusion Equations* (Springer-Verlag, New York/Berlin, 1983).
17. J. A. Trangenstein, *Comput. Mech.* **13,** 343 (1994).
18. J. A. Trangenstein and P. Colella, *Commun. Pure Appl. Math.* **44,** 41 (1991).
19. J. A. Trangenstein and R. B. Pember, *J. Comput. Phys.* **103**(1), 63 (1992).
20. B. van Leer, *J. Comput. Phys.* **32,** 101 (1979).
21. I. Vardoulakis and B. Graf, *Géotechnique* **35,** 299 (1985).